catalysts

MDPI

Article

Fabrication of WS_2/WSe_2 Z-Scheme Nano-Heterostructure for Efficient Photocatalytic Hydrogen Production and Removal of Congo Red under Visible Light

Tsung-Mo Tien [1,*], Yu-Jen Chung [2], Chen-Tang Huang [1] and Edward L. Chen [1,*]

[1] Coastal Water and Environment Center, College of Hydrosphere Science, National Kaohsiung University of Science and Technology, Kaohsiung City 81157, Taiwan
[2] Department of Marine Science, Republic of China Naval Academy, Kaohsiung City 81300, Taiwan
* Correspondence: tmtien@nkust.edu.tw (T.-M.T.); edwardljchen@gmail.com (E.L.C.)

Abstract: In this study, a novel tungsten disulfide/tungsten diselenide (WS_2/WSe_2) heterojunction photocatalyst by a facile hydrothermal process with great capable photocatalytic efficiency for hydrogen evolution from water and organic compound removal was discussed. The WS_2/WSe_2 heterojunction photocatalyst to form heterojunctions to inhibit the quick recombination rate of photo-response holes and electrons is reflected to be a useful method to enhance the capability of photocatalysis hydrogen production. The hydrogen production rate of the WS_2/WSe_2 photocatalyst approach is 3856.7 μmol/g/h, which is 12 and 11 folds the efficiency of bare WS_2 and WSe_2, respectively. Moreover, the excellent photocatalytic performance for Congo Red (*CR*) removal (92.4%) was 2.4 and 2.1 times higher than those of bare WS_2 and WSe_2, respectively. The great photocatalytic efficiency was owing to the capable electrons and holes separation of WS_2/WSe_2 and the construction of Z-scheme heterostructure, which possessed vigorous photocatalytic oxidation and reduction potentials. The novel one-dimensional structure of WS_2/WSe_2 heterojunction shortens the transport pathway of photo-induced electrons and holes. This work provided an insight to the pathway of interfacial separation and transferring for induced charge carriers, which can refer to the interfacial engineering of developed nanocomposite photocatalysts. It possessed great capable photocatalytic efficiency of hydrogen production and organic dye removal. This study offers an insight to the route of interfacial migration and separation for induced charge carriers to generating clean hydrogen energy and solve environmental pollution issue.

Keywords: Z-scheme heterojunction; hydrogen production; photocatalytic; visible light

Citation: Tien, T.-M.; Chung, Y.-J.; Huang, C.-T.; Chen, E.L. Fabrication of WS_2/WSe_2 Z-Scheme Nano-Heterostructure for Efficient Photocatalytic Hydrogen Production and Removal of Congo Red under Visible Light. *Catalysts* **2022**, *12*, 852. https://doi.org/10.3390/catal12080852

Academic Editor: Amr Fouda

Received: 12 July 2022
Accepted: 29 July 2022
Published: 3 August 2022

1. Introduction

Owing to the consecutive development of broad industrialization, the global economy has made significant evolution. For these causes, it is essential to develop suitable methods to obtain energy from renewable sources such as solar energy. In addition, solar energy is a pure and abundant source, gaining increased attention over the last 20 years [1]. Hydrogen could be adopted as a clean replacement to fossil fuel, which presents high energy content and lesser environmental pollution [2]. While solar energy is a renewable resource, photocatalytic decomposition of water to generate hydrogen is a promising route to make clean energy and solve the environmental issues [3,4]. On the other hand, the poor capability of hydrogen evolution, complex fabrication procedure, and high cost of the photocatalysts deeply limit its utilizations. Therefore, great photo-induced capability, no secondary pollution, and low-cost process for decomposing water (H_2O) into hydrogen (H_2), photocatalytic decomposition are the highlights of the present research [5]. In addition, a probable photocatalytic hydrogen evolution route essential wide and vigorous light absorption to generate more amount of charge carriers, and useful electrons and holes

separation efficiency as well as proper energy band gaps to induced the response of reducing H_2O to H_2.

In photocatalysis, the primary points affecting the photocatalytic capability include the visible light application potential, the migration, and separation performance of photogenerated electrons-holes [6]. To develop the photocatalytic process efficiency, many strategies were presented, such as fabricating nano-scale structures, varied morphologies, and synthesizing with semiconductor or co-catalyst semiconductor. It has been noted in photocatalysts that it is critical for a single component to own better photocatalysis capability to benefit the functional need because of its confined high recombination rate of photoexcited electron and hole pairs and light absorption efficiency. Z-scheme photocatalytic activities can apply renewable solar light energy to produce clean hydrogen and environmental pollution treatment, which is reflected to be a probable method to solve environmental and energy issues [7]. Therefore, the formation of heterostructures is proposed because they can combine the benefits of each material and improve the separation rate of photoexcited carries [8]. It is also indicated that the contact surface area of heterojunction interface provides enhancement significantly to the photoresponse capability in the route of photocatalytic redox reaction [9].

Transition metal tungsten sulfides have been broadly researched as excellent semiconductor photocatalysts [10,11]. Because of their outstanding photoelectric capability and particular band gap properties, they possess better potential in the field of photocatalytic activity. As favorable photocatalysts, WS_2 and WSe_2, have been usually studied for photocatalytic hydrogen production owing to their appropriate band gap and proper energy band gap position. Then, the inactive activities of photoinduced charge carries separation confined the photocatalytic hydrogen energy performance of bare WS_2 and WSe_2 component [12]. On the other hand, the rapid recombination of photoexcited charge carriers of bare WS_2 and WSe_2 seriously suppressed its efficient utilization in the environment. Although, no elaborate research has been conducted on the heterostructures of WS_2 and WSe_2 for its potential in photocatalytic capabilities. Accordingly, modulation of the interface charge delivery toward Z-scheme route for excellent redox efficacies and operation of interfacial match for rapid removal of photoinduced electron-holes pairs has become a crucial requirement.

In this case, two necessities are essential to quickly separate the electron-hole pairs on the reduced material and the oxidized material. Moreover, the compact interface of the heterojunction can also enhance the removal of photoinduced charge carriers, improve the lifetime of photoresponse carriers, and advance the reduction of H^+ on the photocatalyst surface. Based on the above studies, the formation of WS_2/WSe_2 heterojunction photocatalyst could be favorable for the powerful separation and transfer of photoexcited charge carriers and for improving the photocatalytic performance. The photocatalytic activity of WS_2/WSe_2 heterojunction photocatalyst was systematically studied by photocatalytic hydrogen evolution and CR removal under visible light irradiation. Our research study will open a new route in designing novel nanocomposites with great photocatalytic performance toward the photo-response hydrogen production rate and the removal of organic environmental pollutants.

2. Results

2.1. Microstructure Characterization

Figure 1 displays the XRD patterns of the WS_2, WSe_2, WS_2/WSe_2-5, WS_2/WSe_2-10, and WS_2/WSe_2-20 samples recorded by combining various amounts of WSe_2. As exhibited in the results, with the addition of WSe_2, the diffraction peak position of the WS_2/WSe_2 does not obviously change, and no other impurity peaks appear. As the counting of WSe_2 is increased from 5 to 20 mg, the XRD analysis of WS_2/WSe_2-X (X = 5, 10, and 20) become increasingly shifted within the range of 13.5° to 14.3° corresponding to (002) planes of WS_2 and WSe_2 (JCPDS 84-1398 and 96-901-2194) [13,14]. The major characteristic peaks of the (002) plane can be observed in the patterns of WS_2/WSe_2-5, WS_2/WSe_2-10, and

WS_2/WSe_2-20. In particular, contrast with the XRD analysis of WSe_2, the overall diffraction intensities of WS_2/WSe_2 heterojunctions were altered to lower peaks (see Figure 1 inset). With the increase of WSe_2 content, the position of the characteristic peaks of the (002) plane in the WS_2/WSe_2-5, WS_2/WSe_2-10, and WS_2/WSe_2-20 patterns gradually shifts toward low 2 theta degree, which proves that the WS_2/WSe_2-5, WS_2/WSe_2-10, and WS_2/WSe_2-20 heterojunctions have been successfully constructed. This result also indicates the successful chemical combination of WSe_2 and WS_2 in WS_2/WSe_2 heterostructure. The results exhibited that the facile hydrothermal process could achieve a heterostructure without the destruction of the lattice structure. UV–Vis was conducted to analyze the optical properties of the samples. Figure 1b displays that the absorption edge of WS_2/WSe_2-X (WS_2/WSe_2-5, WS_2/WSe_2-10, and WS_2/WSe_2-20) is about 450~550 nm, indicating that the WS_2/WSe_2-X impacts well the visible light range. The absorption edge of WS_2/WSe_2-20 heterojunction has a redshift compared to WS_2/WSe_2-5 due to the interaction between WS_2 and WSe_2. It means the generated WS_2/WSe_2-20 nanocomposite displayed the enhanced absorption ability of visible light, which was favorable to generate more photoexcited electrons and holes for beginning redox responses. The band gap (Eg) energies of WS_2/WSe_2-X are estimated by the Tauc equation $((\alpha h\upsilon)^2 = A\ (h\upsilon - Eg)^n)$ [15]. Figure 1b inset reveals that the Eg of WS_2/WSe_2-5, WS_2/WSe_2-10, and WS_2/WSe_2-20 are 2.56, 2.66 and 2.74 eV, respectively.

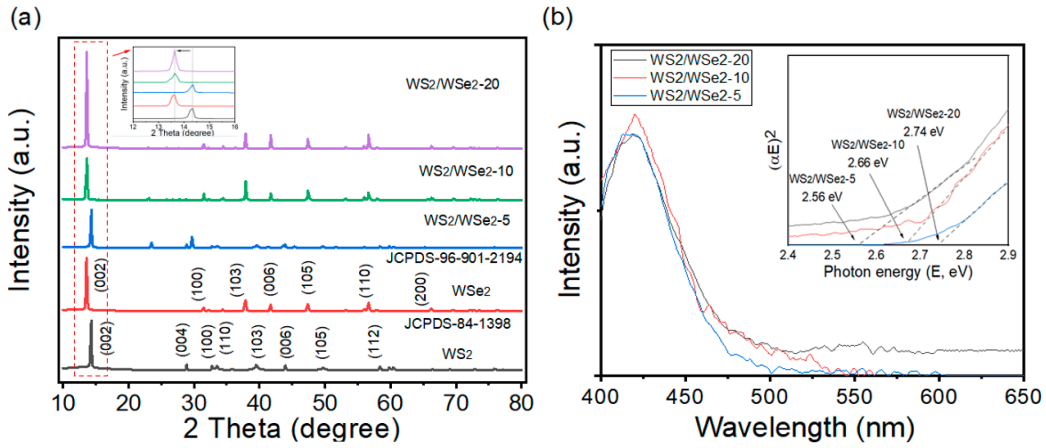

Figure 1. (**a**) XRD patterns of the as-prepared samples; (**b**) UV–vis spectra of WS_2/WSe_2-5, WS_2/WSe_2-10, and WS_2/WSe_2-20 samples; plots of $(\alpha h\upsilon)^2$ versus hυ for the bandgap energies of the photocatalysts in the inset.

The morphology and microstructure of the WS_2/WSe_2-5, WS_2/WSe_2-10, and WS_2/WSe_2-20 samples were also measured by SEM and TEM. Figure 2a,b shows the SEM image of pure WS_2 and WSe_2 samples. It is obvious that the bulk WS_2 and WSe_2 materials are severely agglomerated in the range of average width 20–50 μm. As shown in Figure 2c, the WS_2/WSe_2-20 has a particle size of nearly 3–5 μm, and sphere-like morphology on its surface are developed by the rough stacking of particles. The rough organization of particles contribute not only to volume of space but also to endow support for the firm attaching of WS_2 and WSe_2 samples. Noticeably, compared with WS_2 and WSe_2, the surface of WS_2/WSe_2 reveals obviously loose, which will be profitable for WS_2/WSe_2-20 to serve a better specific surface area and will be easier to combine with other materials. The TEM images of WS_2/WSe_2-20 composites are shown in Figure 2d–i, it could be apparently observed that the WS_2 was combined by a WSe_2 with an evident interface between two materials, implying the presence of a heterojunction structure. In addition, Figure 2e exhibited the HRTEM image of WS_2/WSe_2-20 samples, and the interlayer distances of 0.28 and 0.34 nm were corresponding to the (002) lattice plane of WS_2 and (110) lattice planes of WSe_2, respectively. The elemental of W, S, and Se were smoothly dispersed on the entire composite in EDS mapping (Figure 2f–i), suggesting the presence of WS_2 and WSe_2 in nanocomposites. Moreover, it can be apparently noted that the areas of the elemen-

tal distribution of WS_2 with sphere shape were smaller than that of WSe_2 sample. It also suggested the WSe_2 nanoparticles had adhered to the surface of WS_2, confirming the heterojunction with WS_2/WSe_2 was well fabricated. This heterostructure would mainly expand the contact surface area between WSe_2 and WS_2, thus improving the absorption ability of small molecules (organic pollutants and water molecules) [16,17]. The results reveal that improving the photocatalytic activity of the composite accelerates the separation of charge carriers. Therefore, we confirmed the formation of the WS_2/WSe_2-20 heterostructure.

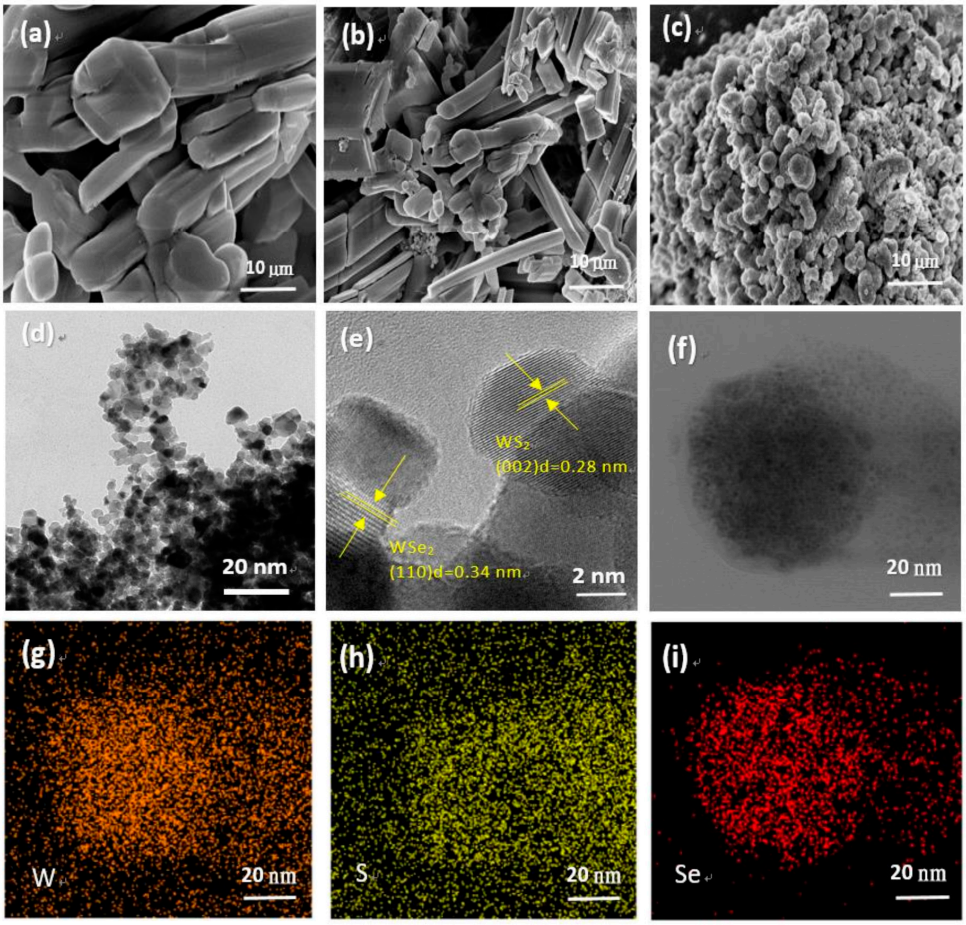

Figure 2. SEM images of (**a**) WS_2, (**b**) WSe_2, and (**c**) WS_2/WSe_2-20, TEM images of (**d**) WS_2/WSe_2-20; HRTEM images (**e**) and element mapping images (**f**–**i**) of WS_2/WSe_2-20.

X-ray photoelectron spectroscopy (XPS) was performed to check the chemical composition and surface element status in the as-prepared WS_2/WSe_2-20 sample. Figure 3 displays the high-resolution XPS spectra of different elements for WSSe-3 sample. As displayed in Figure 3a, the feature peaks of W could be divided into three peaks, among which the feature peaks at 32.1, 34.2, and 37.5 eV refer to the W 4f 7/2, W 4f 5/2, and W 5p 3/2, respectively. In Figure 3b, a high-resolution spectrum of the S 2p peak can be into two peaks of S 2p3/2 and S 2p1/2 spin–orbit doublets at 162.8 and 161.7 eV, implying that S^{2-} existed in the WS_2/WSe_2-20. Then, two divided feature peaks of Se 3d in WS_2/WSe_2-20 examined at 53.8 eV and 54.6 eV can be referred to Se 3d5/2 and Se 3d3/2 (Figure 3c), displaying the chemical status of Se element was Se^{2+}, relative to the former report [13,14]. For the above XPS test events of the as-fabricated photocatalyst, it exhibited that the nanocomposite was well prepared by a facile hydrothermal process and there was a vigorous interaction between WS_2 and WSe_2, which was in good agreement with the XRD results. To check the BET-specific surface area of the nanocomposites, N_2 adsorption–desorption tests were achieved (Table 1). The pore structure and specific surface area of the samples analyze the size of the exposed active area during the photocatalytic activity and have a definite effect

on the photocatalytic efficiency of water splitting to generate hydrogen energy. The specific surface areas of WSe_2, WS_2, and WS_2/WSe_2-20 are 33.6, 23.3, and 68.6 $m^2\ g^{-1}$, respectively, displaying that the specific surface area of WS_2/WSe_2-20 increases significantly after combining with WSe_2. Moreover, compared with WS_2/WSe_2-20 (0.347 $cm^3\ g^{-1}$), the average pore diameter (9.5 nm) of WS_2/WSe_2-20 is improved. On the other hand, it provides to effectively separating the photoexcited charge carries, thus will also demonstrate more active sites for promoting photocatalytic hydrogen evolution capability [18].

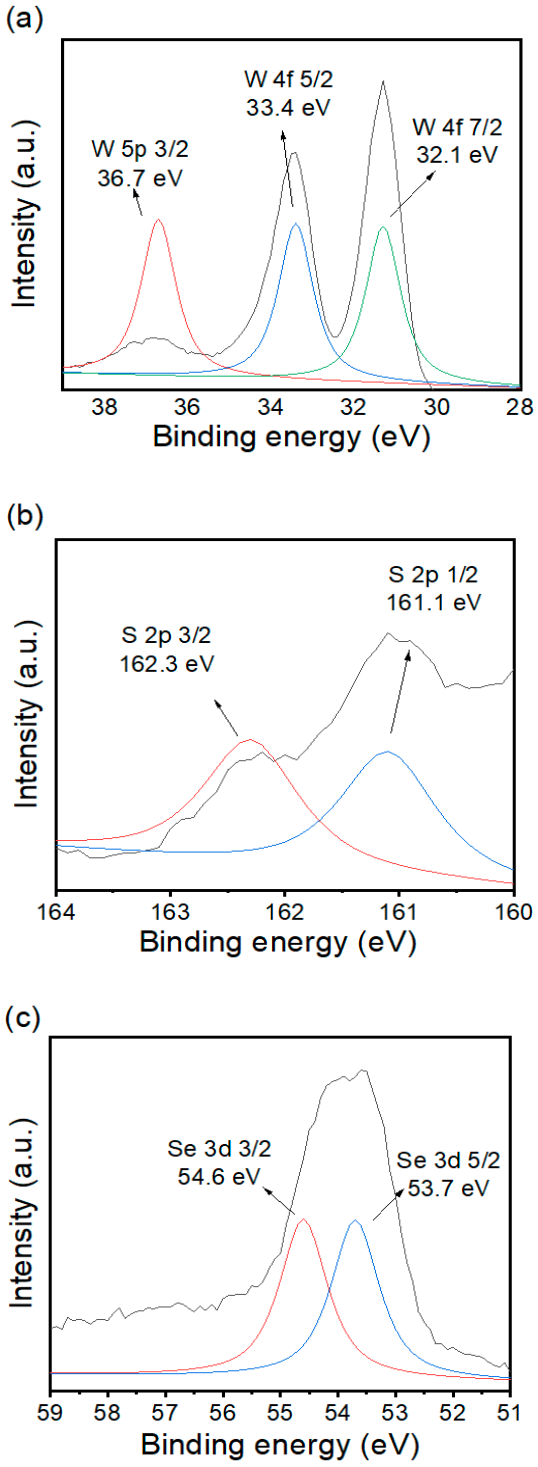

Figure 3. XPS survey spectra of WS_2/WSe_2. High-resolution XPS spectra of the (**a**) W 4f, (**b**) S 2p, and (**c**) Se 3d.

Table 1. The physical adsorption factors of the photocatalysts of WS_2, WSe_2, and WS_2/WSe_2-20 were measured three times.

Samples	Specific Surface Area (m^2/g, BET) [a]	Total Pore Volume (cm^3/g, BET) [b]	Average Pore Diameter (nm, BJH)[b]
WSe_2	33.6±5	0.182±0.02	38.4±5
WS_2	23.3±5	0.113±0.02	48.5±5
WS_2/WSe_2-20	68.6±5	0.347±0.02	9.5±3

[a] Received from BET analysis. [b] Relative pressure (P/P_0) was 0.99.

2.2. Hydrogen Production Behavior

As displayed in Figure 4a,b, the hydrogen production rate of WS_2/WSe_2-20 enhanced by 13 and 12 times of WS_2 and WSe_2, respectively. The total production of H_2 followed the order: WS_2/WSe_2-20 (3856.7 μmol g^{-1}) > WS_2/WSe_2-10 (3546.2 μmol g^{-1}) > WS_2/WSe_2-5 (2743.5 μmol g^{-1}) > WSe_2 (334.6 μmol g^{-1}) > WS_2 (315.4 μmol g^{-1}). Adding excessive photocatalyst, owing to the WS_2/WSe_2-20 nanocomposites aggregation, suggests a reduced surface area of WS_2/WSe_2-20 and thus hindering the transfer ability of the charge carries [19]. However, all WS_2/WSe_2 heterojunction photocatalyst shows improved photocatalytic hydrogen evolution efficiency, implying that the electron localization and boost interaction at the WS_2/WSe_2-20 sample interface capably accelerate charge transfer and separation ability. Moreover, excessive nanocomposites may result in recombination for electron-hole pairs, hence decreasing the photocatalytic efficiency. By contrast, a slight amount of photocatalyst will cause the interface between the WS_2 and WSe_2 too restricted to separate and transport the photoexcited electrons and holes pairs, which cannot mainly suppress the recombination rate of photoexcited charge carriers. As exhibited in Figure 4c, with the adding of WS_2/WSe_2-20 heterostructures, the amount of hydrogen production enhances gradually until the amount of WS_2/WSe_2-20 nanocomposites approaches 30 mg. Moreover, the hydrogen production rate is gradually suppressed with increasing WS_2/WSe_2-20 nanocomposites. This reveals that the water molecules in the solution could be adsorbed by the photocatalysts and mainly employed when the amount of WS_2/WSe_2-20 nanocomposites is suitable. A mass of WS_2/WSe_2-20 nanocomposites over 30 mg results in excess photocatalyst stock in the mixture solution, inhibiting efficient charge carries transport and photon adsorption of the nanocomposite and hence decreasing the amount of photons on the sample surface and suggesting decreased hydrogen evolution efficiency. To investigate the reusability and the chemical stability of WS_2/WSe_2-20 nanocomposite in hydrogen evolution rate, cycling test was carried out at the same situations. As displayed in Figure 4d, the number of hydrogen generated in the fourth cycle was obviously decreased compared to the original case. The hydrogen production rate endured at nearly 96.2% compared to the original matter. When 20 mg WS_2/WSe_2-20 nanocomposites were increased again, the number of hydrogen production rate was evidently increased, implying that the photocatalysis of WS_2/WSe_2-20 nanocomposites was the primary factor for the increase in hydrogen production. At the end of the cycling performance analysis, the XRD analysis of the sample was conducted again. As displayed in Figure 4e, the crystal structure and morphology of WS_2/WSe_2-20 do not change obviously before and after the cycling test, which further demonstrates the excellent chemical stability and repeatability of the nanocomposites in photocatalytic hydrogen evolution efficiency. Therefore, the hydrogen evolution rate of the WS_2 mixtures is 315.4 lmol g^{-1} h^{-1}, which is significantly lower than the WS_2/WSe_2-X heterojunctions. The above results implied that the as-prepared WS_2/WSe_2-20 nanocomposite can be applied as a potential hydrogen generating photocatalysts.

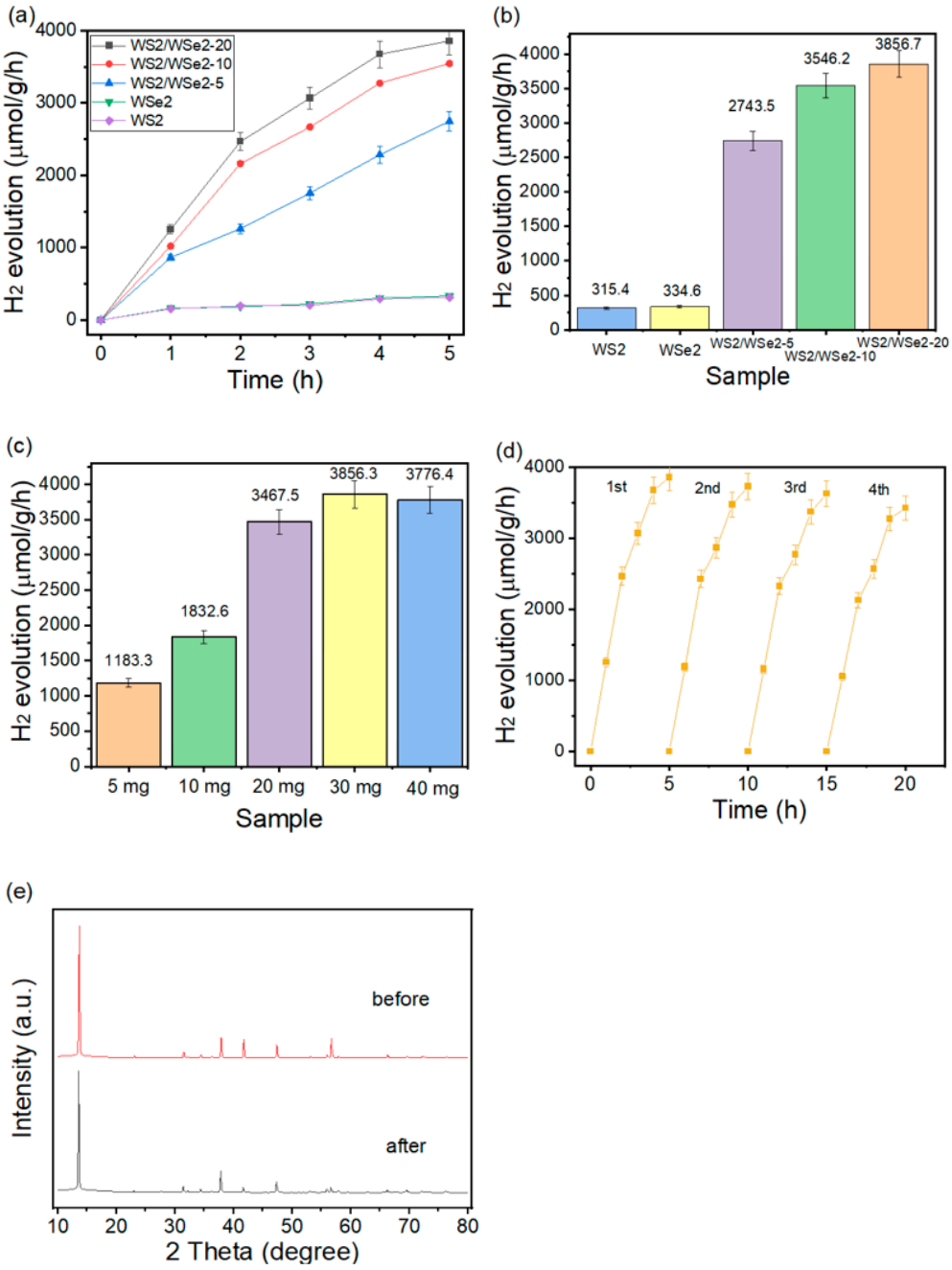

Figure 4. H_2 evolution of (**a**) WS_2, WSe_2, and WS_2/WSe_2-20 and H_2 production comparison of (**b**) WS_2/WSe_2-5, WS_2/WSe_2-10, and WS_2/WSe_2-20. (**c**) H_2 production with various usage amounts of WS_2/WSe_2-20. (**d**) H_2 production of the cycling performance, (**e**) XRD analysis of WS_2/WSe_2-20 before and after the hydrogen production activity.

2.3. CR Degradation Behavior

It can be noted from Figure 5a that the feature absorption intensity of CR at 346 and 497 nm apparently decreased with increasing irradiation time, confirming that CR was practically degraded by the WS_2/WSe_2-20 nanocomposite. The above photocatalytic results revealed that decreased preparation of WS_2/WSe_2-20 nanocomposite accelerated the separation rate and space charge transfer distance of photoexcited charge carries, thus improving the photodegradation performance [20]. To further check the photodegradation performance of the photocatalyst, the photodegradation of the CR pollutant was conducted. Figure 5b displays the adsorption equilibrium test in dark for 20 min, the adsorption number of CR via all

photocatalysts is negligible. The blank test shows that the self-photocatalytic of CR could be ignored, indicating that the property of CR is stable in the photocatalytic activity. WS_2 and WSe_2 have poor capability for CR removal with visible light irradiation, which are 38.6%, and 46.5% within 60 min, respectively. Noticeably, WS_2/WSe_2-5, WS_2/WSe_2-10, and WS_2/WSe_2-20 approaches the better photocatalytic capability for CR removal, which is 82.5%, 88.3%, and 92.4%. Corresponding to photocatalytic hydrogen evolution, the operation series of photocatalytic MB removal is as follows: WS_2/WSe_2-20 > WS_2/WSe_2-10 > WS_2/WSe_2-5 > WSe_2 > WS_2. Moreover, the CR degradation performance of WS_2/WSe_2-20 is 2.4 and 2 times that of WS_2 and WSe_2 samples, respectively. Figure 5c displays the cycling experiment of WS_2/WSe_2-20 for photo degradation CR pollutant. The photodegradation efficiency decreases slightly from 92.4% to 82.1% after six repeated cycling tests, which verify that WS_2/WSe_2-20 has excellent stability and repeatability in the photo degradation CR process.

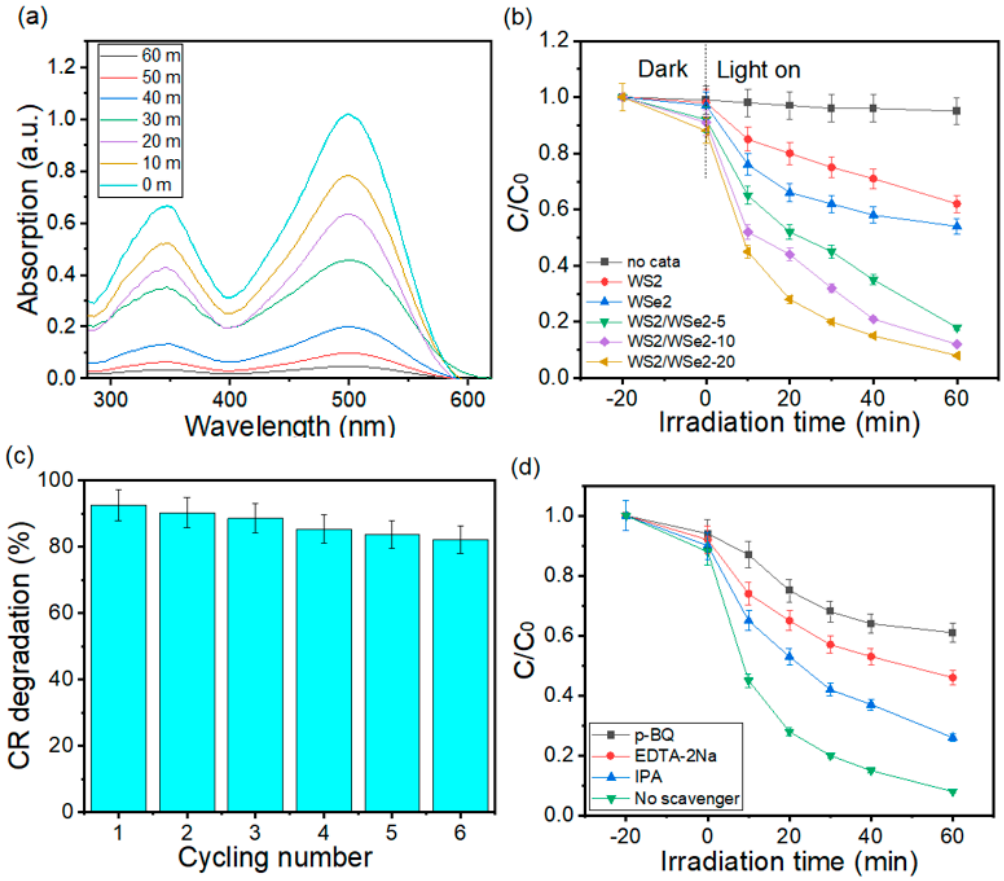

Figure 5. *Cont.*

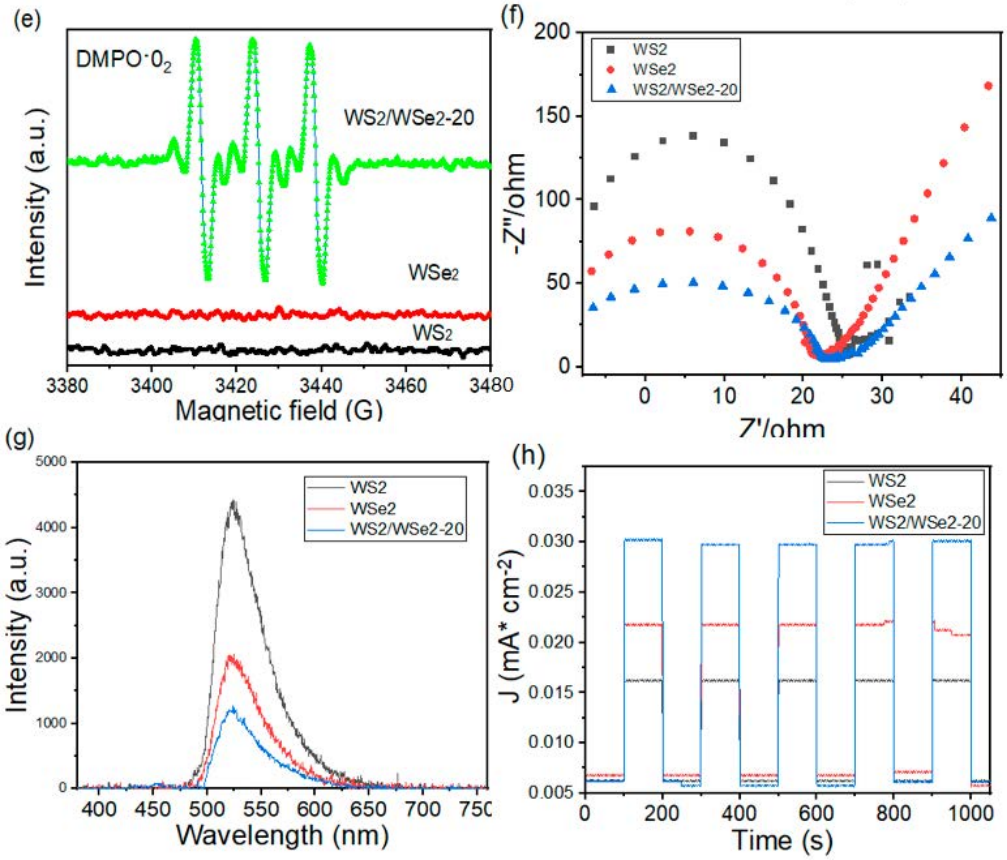

Figure 5. (**a**) CR spectra adsorption changes during the photocatalytic process, (**b**) Photodegradation curves of CR, (**c**) cycling test for WS_2/WSe_2-20 sample, (**d**) reactive species trapping tests, and (**e**) DMPO spin-trapping ESR spectra of DMPO-O_2^-. (three repeat tests to estimate error bars), (**f**) electrochemical impedance spectroscopy of the as-fabricated photocatalysts, (**g**) photoluminescence spectroscopy (PL), and (**h**) transient photocurrent curves of WS_2, WSe_2, and WS_2/WSe_2-20.

To further confirm the active species of photocatalyst, the influences of various capture agents during the photocatalytic activity were proved. The capture agents are isopropanol (IPA) for OH, benzoquinone (BQ) for O_2^-, and EDTA-2Na for h^+. When IPA is adopted into the photocatalytic activity, the photocatalytic reaction slightly diminishes, implying that OH has weak effect on CR removal in Figure 5d. On the other hand, when BQ or EDTA-2Na is adopted into this test, the photocatalytic efficiency decreases obviously, implying that h^+ and O_2^- are the major active species [21]. Furthermore, the ESR analysis (Figure 5e) indicates that WS_2/WSe_2-20 has the DMPO-O_2^- adduct signal, which also verifies that O_2^- exists in the photocatalytic activity. Electrochemical impedance spectroscopy (EIS) was performed to check the transportation and charge carries separation rate of nanocomposite surface [22]. In Figure 5f, the Nyquist semicircle radius of WS_2/WSe_2-20 is significantly smaller than that of pure WS_2 and WSe_2, verifying that the transfer resistance of photoexcited electrons and holes in WS_2/WSe_2-20 is the smallest among these catalysts. It was indicated that the WS_2/WSe_2-20 improved the charge transfer ability for composite. To further study the charge carries transfer and separation capability of the nanocomposites, a PL measurement was conducted. Figure 5g exhibits the PL spectra of WS_2, WSe_2, and WS_2/WSe_2-20 under 420 nm excitation. Compared with WS_2 and WSe_2, the PL peak intensity of WS_2/WSe_2-20 decreases significantly. The PL intensity decreased in the order of WS_2/WSe_2-20 < WSe_2< WS_2, clearly describing that WS_2/WSe_2-20 sample presented the better the electrons and holes separating capability, which was in good agreement with above EIS analysis results. The result demonstrated that the WS_2/WSe_2-20 nanocomposite can mainly transfer photoexcited electrons and holes to inhibit their recombination ability.

As shown in Figure 5h, these results demonstrate that the bare WS_2 and WSe_2 present a poor transient photocurrent response with visible light irradiation for several on–off cycles. This low photocurrent response of bare components can be attributed to the quick recombination rate of the photoexcited charge carriers. WS_2/WSe_2-20 exhibits excellent photocurrent intensity than bare WS_2 and WSe_2, which implies enhanced charge carrier separation and migration in the heterojunction photocatalyst. All above results apparently verify that the photoexcited electrons and holes in WS_2/WSe_2-20 could be effectively transferred and separated.

Accordingly, the above results of different data analysis and previous investigations, the probable photoexcited charge carries transport paths for the enhanced photocatalytic efficiency are recommended in Figure 6. According to the prior study, the bandgap value of the made WSe_2 sample was 1.76 eV, and the bandgap value of WS_2 was 1.92 eV [23,24]. The VB-XPS analysis was also concluded to establish the VB levels of WSe_2 and WS_2, and the results are displayed in Figure 6a–c. Obviously, the VB levels of WSe_2 and WS_2 were calculated to be 2.03 and 1.28 V, respectively. Furthermore, the CB potential of WSe_2 and WS_2 were calculated by the formula ($Eg = E_{VB} - E_{CB}$), which were 0.27 eV and −0.64 eV, respectively. Both WS_2 and WSe_2 were induced and excited charge carries on their valence bands (VB) and conduction bands (CB) under visible light irradiation conditions owing to their narrow band energies. Accordingly, the photo-induced charge carries were transferred from VB and CB of WS_2 to the consistent positions of WSe_2 due to band gap energy difference. Because of the nanocomposites, the confined charge carries with high energy enhanced in the heterostructure can be transported rapidly to the photocatalyst surface across the tunneling influence to contribute to the chemical redox activity. Therefore, some section of the photoexcited electrons and holes could also directly contribute to the redox reaction owing to the nanocomposite developed in heterojunction WS_2/WSe_2-20 nanomaterials. This result was similar to the previous studies [25–27]. The photoexcited charges collected on surface of photocatalyst can directly contribute to the reduction of H_2O to H_2 under the hydrogen production process. Then the nanocomposite was the main active site for reaction. For the photodegradation process of CR, the electrons on the surface of photocatalyst respond to O_2 to generate O_2^- and H^+ is reduced to H_2, which was the primary active site for degradation of CR and hydrogen production. At the same time, the holes created as a result of directly oxidation on CR organic molecule cause H_2O to generate OH. This is in good agreement with the ESR trapping results. The possible mechanism for the enhanced photocatalytic activity from above experiment analysis were as follows: (1) The extended specific surface area was profitable for creating more active species and better photoactivity; (2) the improved visible light absorption range can improve the light capture efficiency to promote photocatalytic application; (3) the synthesized heterostructure with preferred interface contact offered better transfer pathway for charge carries, which can promote photoexcited electrons and holes separation capability to enhance the photocatalytic efficiency.

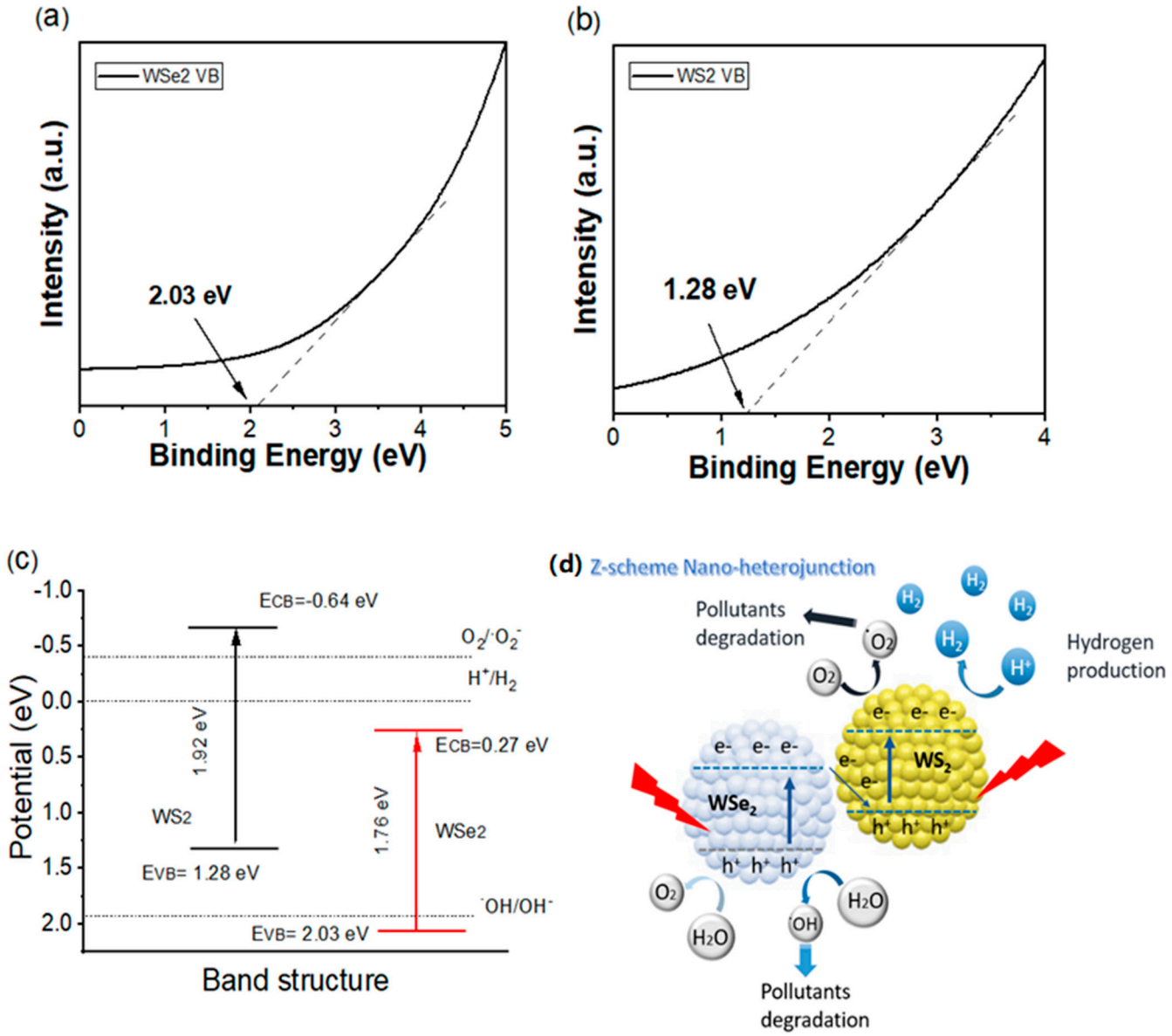

Figure 6. UPS spectrum (**a**) WSe_2, (**b**) WS_2, and (**c**) band structure diagram of WS_2/WSe_2, (**d**) Schematic diagram of the proposed Z-Scheme photoelectron mechanism of WS_2/WSe_2 photocatalytic system under visible light illumination.

3. Materials and Methods

3.1. Preparation of Materials

Sodium tungstate dehydrate ($Na_2WO_4{\cdot}2H_2O$, ≧ 99%), the L-cysteine ($C_3H_7NO_2S$, ≧ 97%), tungstate selenium powder (WSe_2, ≧ 99.5%), hydrochloric acid (HCl, ≧ 37%), Congo Red (CR), and ethanol (C_2H_5OH, ≧ 99.7%) were obtained from Sigma-Aldrich (St. Louis, MO, USA). Deionized (DI) water (resistivity ≧ 18.0 MΩ) was used as experimental water source in further experimental procedures. All the reagents were applied without any further purification.

3.2. Synthesis

The water-soluble WS_2/WSe_2 heterojunction photocatalyst was synthesized by a facile hydrothermal process. First, 65 mg of $Na_2WO_4{\cdot}2H_2O$ was added to 20 mL of DI water with stirred for 10 min. Afterwards, 0.1 M HCl was used to adjust the pH to 6.8. Next, 25 mg of L-cysteine, tungstate selenium powder and 50 mL of water were added into the mixture solution by stirring for 15 min. The mixed solution was transferred to a Teflon-lined

autoclave after vigorous stirring for 20 min and kept at 180 °C for 36 h in an oven. After the reaction was completed, the precipitates were centrifuged for 20 min at the 10,000 rpm. The resulting product was washed with alcohol, deionized water, and acetone several times. The washed precipitates were dried in a vacuum drying oven (overnight). Eventually, a series of WS_2/WSe_2 nanocomposite with diverse WSe_2 mass ratios of 5 wt%, 10 wt% and 20 wt% was arranged, and served as WS_2/WSe_2-5, WS_2/WSe_2-10, and WS_2/WSe_2-20, respectively. As displayed in Scheme 1, the fabrication of WS_2/WSe_2 heterojunction was described by the hydrothermal process.

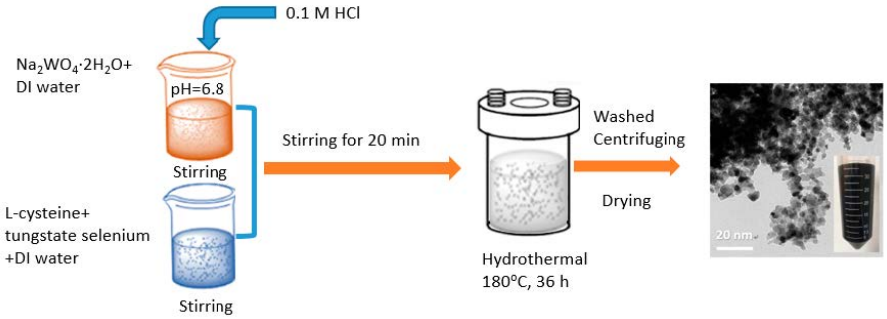

Scheme 1. The rough synthetic route of WS_2/WSe_2 composites.

3.3. Characterization

The field emission scanning electron microscopy (SEM) and transmission electron microscopy (TEM) were carried out to observe the microstructure and morphology of the samples. The chemical composition of the samples carried out by X-ray photoelectron spectroscopy (Thermo Fisher Scientific, Waltham, MA, USA) was also recorded. Brunauer–Emmett–Teller (BET) method was used to measure the pore volume, surface area, and pore distribution. The crystal phase and structure of the as-fabricated samples were analyzed with a powder X-ray diffractometer (Bruker D8 Advance) applying Cu Ka radiation (k = 0.154168 nm). The optical spectra were recorded by a UV–Vis reflectance spectrophotometer (Hitachi U-4100) and photoluminescence (PL). Photochemical property was determined on an electrochemical workstation with a 0.2-M Na_2SO_4 solution as the electrolyte. Electron spin resonance (ESR) signals of the radicals captured were performed with visible light activity on a Bruker A300 spectrometer.

3.4. Photocatalytic Hydrogen Evolution Tests

The hydrogen production test was checked by quantitatively and periodically extracting gas from a reactor with visible light irradiation. Driving nitrogen to replace the air in the reactor was sufficient to assure atmospheric pressure in the reactor. In this study, 10 mg of the photocatalyst was added to a mixture solution (50 mL) including 30 mmol Na_2S and 20 mmol Na_2SO_3 as a sacrificial agent. The mixture solution was evacuated to extract air entirely before activities. The pumping light source adopted was a 300 W Xe lamp with $\lambda > 420$ nm filter. The mixture solution was stirred consecutively under the reaction. The amount of hydrogen production during light activity was determined using a gas chromatography (GC-7890, TCD) coupled with a thermal conductivity detector to measure the evolution of H_2.

3.5. Photocatalytic Activity Experiments

The photocatalytic capability of the prepared nanocomposite samples was used by their removal efficiency of an organic compound (CR) in aqueous solution by applying 300 W Xe lamp as a light source. Before photoreactions, 10 mg as-prepared sample was dispersed in 100 mL (10 ppm) CR solution and the reaction solution was continuously stirred for 30 min under darkness to achieve the adsorption–desorption balance between organic compound and photocatalysts surface. Accordingly, the reaction solution was irradiated with a Xe lamp source, and then 5 mL suspension was taken out at the same

conditions. After removing the photocatalyst by centrifugation, the concentration of CR was determined by the UV–Vis spectrophotometer. Moreover, trapping tests were further performed to photoexcited active species by using particular volume of scavengers 1,4-benzoquinone (BQ), EDTA-2Na, and 2-propanol (IPA) in the reaction system.

4. Conclusions

In conclusion, a novel Z-scheme WS_2/WSe_2 heterojunction photocatalyst were synthesized by the hydrothermal process, which leads to the formation of intimated interfacial contact and heterojunction for energy conversion and environmental remediation. This work demonstrated that the as-fabricated WS_2/WSe_2 proved beneficial to the migration of photoexcited charge carries, and can further enhance its photocatalytic hydrogen production activity and CR degradation with visible light irradiation. In addition, the photocatalytic efficiency of WS_2/WSe_2-20 rises to 3856.7 μmol g^{-1} h^{-1} (the H_2 production rate) and 92.4% (photocatalytic efficiency of CR degradation), which were 12 and 2.4 times higher than that of bare WS_2, respectively. The outstanding improvement of photocatalytic system might be due to the nanocomposite structure and the heterojunction effect between WS_2 and WSe_2. Moreover, the WS_2/WSe_2-20 nanocomposite exhibited better reusability and chemical stability. This study not only shows the improved light absorption efficiency of the prepared material, but also shows more photocatalytic active sites which shortens the electrons transport path. This study provides valuable reference to Z-scheme heterojunction photocatalysts in water splitting field, and the further exploration on photocatalytic mechanism for potential sustainable energy production in the future.

Author Contributions: Writing—original draft, methodology, T.-M.T.; writing—review and editing, E.L.C.; data curation, formal analysis, Y.-J.C.; funding acquisition, Y.-J.C.; writing—review and editing, T.-M.T.; validation, C.-T.H.; resources, T.-M.T.; formal analysis, data collection, Y.-J.C.; and C.-T.H.; conceptualizations, writing—review and editing, E.L.C.; supervision, investigation E.L.C.; supervision, project administration. T.-M.T. All authors have read and agreed to the published version of the manuscript.

Funding: This research received no external funding.

Data Availability Statement: Not applicable.

Acknowledgments: The MOST and the NKUST are gratefully acknowledged for their general support. The authors gratefully acknowledge the use of HRTEM equipment belonging to the Instrument Center of National Cheng Kung University.

Conflicts of Interest: The authors declare no conflict of interest.

References

1. Mersel, M.A.; Fodor, L.; Pekker, P.; Makó, É.; Horváth, O. Effects of Preparation Conditions on the Efficiency of Visible-Light-Driven Hydrogen Generation Based on Ni(II)-Modified $Cd_{0.25}Zn_{0.75}S$ Photocatalysts. *Molecules* **2022**, *27*, 4296. [CrossRef] [PubMed]
2. Irfan, M.; Ahmad, I.; Shukrullah, S.; Hussain, H.; Atif, M.; Legutko, S.; Petru, J.; Hatala, M.; Naz, M.Y.; Rahman, S. Construction of 0D/2D Schottky Heterojunctions of ZnO and Ti_3C_2 Nanosheets with the Enriched Transfer of Interfacial Charges for Photocatalytic Hydrogen Evolution. *Materials* **2022**, *15*, 4557. [CrossRef] [PubMed]
3. Chen, L.J. Tunable photoluminescence emission from Cadmium Tellurium nanorods with ethylenediamine template-assistance at a low temperature. *Mater. Lett.* **2013**, *101*, 83.
4. Hao, D.; Liu, Y.; Gao, S.; Arandiyan, H.; Bai, X.; Kong, Q.; Wei, W.; Shen, P.K.; Ni, B.J. Emerging artificial nitrogen cycle processes through novel electrochemical and photochemical synthesis. *Mater. Today* **2021**, *46*, 212–233. [CrossRef]
5. Cai, M.; Cao, S.; Zhuo, Z.; Wang, X.; Shi, K.; Cheng, Q.; Xue, Z.; Du, X.; Shen, C.; Liu, X.; et al. Fabrication of Ni_2P Cocatalyzed CdS Nanorods with a Well-Defined Heterointerface for Enhanced Photocatalytic H_2 Evolution. *Catalysts* **2022**, *12*, 417. [CrossRef]
6. Vadivel, D.; Sturini, M.; Speltini, A.; Dondi, D. Tungsten Catalysts for Visible Light Driven Ofloxacin Photocatalytic Degradation and Hydrogen Production. *Catalysts* **2022**, *12*, 310. [CrossRef]
7. Zhurenok, A.V.; Markovskaya, D.V.; Gerasimov, E.Y.; Vokhmintsev, A.S.; Weinstein, I.A.; Prosvirin, I.P.; Cherepanova, S.V.; Bukhtiyarov, A.V.; Kozlova, E.A. Constructing g-C_3N_4/$Cd_{1-x}Zn_xS$-Based Heterostructures for Efficient Hydrogen Production under Visible Light. *Catalysts* **2021**, *11*, 1340. [CrossRef]
8. Chen, L.J.; Dai, J.H. Growth, morphological and optical characteristics of ZnSSe nanorods. *Opt. Mater.* **2017**, *64*, 356.

9. Yin, S.; Liu, S.; Yuan, Y.; Guo, S.; Ren, Z. Octahedral Shaped $PbTiO_3$-TiO_2 Nanocomposites for High-Efficiency Photocatalytic Hydrogen Production. *Nanomaterials* **2021**, *11*, 2295. [CrossRef]
10. Shahabuddin, S.; Mehmood, S.; Ahmad, I.; Sridewi, N. Synthesis and Characterization of 2D-WS_2 Incorporated Polyaniline Nanocomposites as Photo Catalyst for Methylene Blue Degradation. *Nanomaterials* **2022**, *12*, 2090. [CrossRef]
11. Chen, I.W.P.; Lai, Y.M.; Liao, W.S. One-Pot Synthesis of Chlorophyll-Assisted Exfoliated MoS_2/WS_2 Heterostructures via Liquid-Phase Exfoliation Method for Photocatalytic Hydrogen Production. *Nanomaterials* **2021**, *11*, 2436. [CrossRef] [PubMed]
12. Luo, Z.; Li, Y.; Guo, F.; Zhang, K.; Liu, K.; Jia, W.; Zhao, Y.; Sun, Y. Carbon Dioxide Conversion with High-Performance Photocatalysis into Methanol on $NiSe_2$/WSe_2. *Energies* **2020**, *13*, 4330. [CrossRef]
13. Varadwaj, P.R.; Varadwaj, A.; Marques, H.M.; Yamashita, K. Chalcogen Bonding in the Molecular Dimers of WCh_2 (Ch = S, Se, Te): On the Basic Understanding of the Local Interfacial and Interlayer Bonding Environment in 2D Layered Tungsten Dichalcogenides. *Int. J. Mol. Sci.* **2022**, *23*, 1263. [CrossRef] [PubMed]
14. Niu, Y.; Gonzalez-Abad, S.; Frisenda, R.; Marauhn, P.; Drüppel, M.; Gant, P.; Schmidt, R.; Taghavi, N.S.; Barcons, D.; Molina-Mendoza, A.J.; et al. Thickness-Dependent Differential Reflectance Spectra of Monolayer and Few-Layer MoS_2, $MoSe_2$, WS_2 and WSe_2. *Nanomaterials* **2018**, *8*, 725. [CrossRef] [PubMed]
15. Deshmukh, S.M.; Patil, S.S.; Babar, S.B.; Alshehri, S.; Ghoneim, M.M.; Tamboli, A.M.; Lam, N.H.; Truong, N.T.N.; Kim, C.D.; Tamboli, M.S.; et al. TiO_2–SnO_2 Nanocomposites for Photocatalytic Environmental Remediation under UV-Light. *Metals* **2022**, *12*, 733. [CrossRef]
16. Shehab, M.A.; Sharma, N.; Valsesia, A.; Karacs, G.; Kristály, F.; Koós, T.; Leskó, A.K.; Nánai, L.; Hernadi, K.; Németh, Z. Preparation and Photocatalytic Performance of TiO_2 Nanowire-Based Self-Supported Hybrid Membranes. *Molecules* **2022**, *27*, 2951. [CrossRef]
17. Chen, L.J.; Chuang, Y.J.; Chen, C. Surface passivation assisted lasing emission in the quantum dots doped cholesteric liquid crystal resonating cavity with polymer template. *RSC Adv.* **2014**, *4*, 18600. [CrossRef]
18. Deshmukh, S.M.; Arbuj, S.S.; Babar, S.B.; Shaikh, S.F.; Tamboli, A.M.; Truong, N.T.N.; Kim, C.D.; Khetre, S.M.; Tamboli, M.S.; Bamane, S.R. Environmentally Benign Organic Dye Conversion under UV Light through TiO_2-ZnO Nanocomposite. *Metals* **2021**, *11*, 1787. [CrossRef]
19. Shelke, H.D.; Machale, A.R.; Survase, A.A.; Pathan, H.M.; Lokhande, C.D.; Lokhande, A.C.; Shaikh, S.F.; Rana, A.H.S.; Palaniswami, M. Multifunctional Cu_2SnS_3 Nanoparticles with Enhanced Photocatalytic Dye Degradation and Antibacterial Activity. *Materials* **2022**, *15*, 3126. [CrossRef] [PubMed]
20. Nada, E.A.; El-Maghrabi, H.H.; Raynaud, P.; Ali, H.R.; El-Wahab, S.A.; Sabry, D.Y.; Moustafa, Y.M.; Nada, A.A. Enhanced Photocatalytic Activity of WS_2/TiO_2 Nanofibers for Degradation of Phenol under Visible Light Irradiation. *Inorganics* **2022**, *10*, 54. [CrossRef]
21. Xu, F.; Hu, C.; Zhu, D.; Wang, D.; Zhong, Y.; Tang, C.; Zhou, H. One-Step Hydrothermal Synthesis of Nanostructured $MgBi_2O_6$/TiO_2 Composites for Enhanced Hydrogen Production. *Nanomaterials* **2022**, *12*, 1302. [CrossRef] [PubMed]
22. Safri, A.; Fletcher, A.J. Effective Carbon/TiO_2 Gel for Enhanced Adsorption and Demonstrable Visible Light Driven Photocatalytic Performance. *Gels* **2022**, *8*, 215. [CrossRef] [PubMed]
23. Edelberg, D.; Rhodes, D.; Kerelsky, A.; Kim, B.; Wang, J.; Zangiabadi, A.; Kim, C.; Abhinandan, A.; Ardelean, J.; Scully, M.; et al. Approaching the Intrinsic Limit in Transition Metal Diselenides via Point Defect Control. *Nano Lett.* **2019**, *19*, 4371. [CrossRef]
24. Brasington, A.; Golla, D.; Dave, A.; Chen, B.; Tongay, S.; Schaibley, J.; LeRoy, B.J.; Sandhu, A. Role of defects and phonons in bandgap dynamics of monolayer WS_2 at high carrier densities. *J. Phys. Mater.* **2021**, *4*, 015005. [CrossRef]
25. Chen, L.J.; Chuang, Y.J. Quaternary Semiconductor Derived and formation mechanism by non-vacuum Route from Solvothermal Nanostructures for High-Performance application. *Mater. Lett.* **2013**, *91*, 372. [CrossRef]
26. Hussien, M.S.A.; Bouzidi, A.; Abd-Rabboh, H.S.M.; Yahia, I.S.; Zahran, H.Y.; Abdel-wahab, M.S.; Alharbi, W.; Awwad, N.S.; Ibrahim, M.A. Fabrication and Characterization of Highly Efficient As-Synthesized WO_3/Graphitic-C_3N_4 Nanocomposite for Photocatalytic Degradation of Organic Compounds. *Materials* **2022**, *15*, 2482. [CrossRef]
27. Wang, J.; Yang, S. Superior Degradation Performance of Nanoporous Copper Catalysts on Methyl Orange. *Metals* **2021**, *11*, 913. [CrossRef]